Atomic Spectroscopy

Article

Classification of Heat-treated Microstructures of TC4 Titanium Alloy Using Fiber-optic Laser-induced Breakdown Spectroscopy (FO-LIBS)

Haoyu Guan,[a] Dan Feng,[a,*] Yuanbin Wang,[a] Nan Ma,[a] and Minchao Cui [b,c,*]

[a] Northwestern Polytechnical University, Xi'an 710072, P. R. China

[b] National Innovation Institute of Digital Design and Manufacturing, Wuhan 430205, P. R. China

[c] Shenzhen Cyborg Robot Co., Ltd., Shenzhen 518054, P. R. China

Received: *December 30, 2025;* ***Revised:*** *January 30, 2026;* ***Accepted:*** *January 31, 2026;* ***Available online:*** *January 31, 2026.*

DOI: 10.46770/AS.2025.291

ABSTRACT: TC4 is a representative titanium alloy that has been widely used in the manufacture of critical aerospace components. Its mechanical properties can be significantly enhanced through appropriate heat-treatment processes. These enhancements are fundamentally attributed to heat-treatment-induced changes in the microstructural characteristics. Conventional microstructural characterization techniques are capable of directly revealing microstructural morphology and phase constituents. However, these methods are typically destructive and suffer from low inspection efficiency. To enable rapid and in situ identification of different heat-treated microstructural states in titanium alloys, this study exploits the matrix effects inherent to fiber-optic laser-induced breakdown spectroscopy (FO-LIBS) as discriminative features and proposes a LIBS-based spectral classification framework combining principal component analysis (PCA) and support vector machine (SVM). Random pulse-to-pulse fluctuations are mitigated through intra-spot multi-pulse averaging, followed by feature extraction using PCA. On this basis, an SVM classifier is constructed, with model performance evaluated via cross-validation and quantitatively assessed using confusion matrices. The results demonstrate that, compared with pulse-level spectral classification, samples subjected to intra-spot averaging exhibit markedly improved separability in the low-dimensional principal component space. Using the proposed model, classification accuracies of 100% and 99.8% are achieved for titanium alloy samples subjected to four and eight different heat-treatment conditions, respectively. These findings indicate that, when integrated with data-driven modeling strategies, LIBS shows strong potential for the rapid identification of material microstructural states.

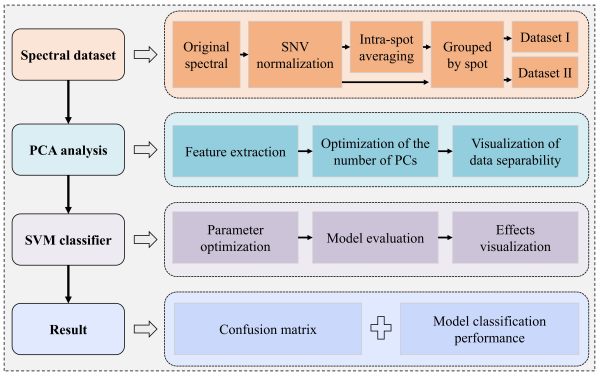

INTRODUCTION

Titanium alloys are well known for their high strength, excellent toughness, superior corrosion resistance, and good thermal stability. Owing to their high strength-to-weight ratio, titanium alloys are widely used in the aerospace industry, particularly in the fabrication of components such as compressor blades, fan casings, and turbine disks[1, 2]. Numerous studies have demonstrated that appropriate heat-treatment processes can effectively modify the mechanical and chemical properties of titanium alloys. The fundamental reason for the pronounced influence of heat treatment lies in its ability to alter both the microstructural characteristics of the alloy. Consequently, the primary objective of heat treatment and thermochemical processing is to transform the initial microstructure into a target microstructure, thereby achieving a balance of properties required for specific applications[3].

At present, the characterization of heat-treated titanium alloy

microstructures primarily relies on conventional materials characterization techniques, including optical microscopy (OM)[4], scanning electron microscopy (SEM)[5], electron backscatter diffraction (EBSD)[6], and X-ray diffraction (XRD)[7]. These methods can reveal the microstructural morphology, phase constitution, and crystallographic characteristics of titanium alloys across multiple length scales, offering high accuracy and reliability in elucidating microstructural evolution during heat-treatment processes. However, these techniques are generally destructive and time-consuming, making it difficult to meet the requirements for rapid, in situ, and nondestructive evaluation of material microstructures under in-service conditions. Consequently, there is a clear need to develop alternative approaches that enable fast identification of different heat-treated titanium alloy microstructural states without compromising material integrity.

Laser-induced breakdown spectroscopy (LIBS) is a noninvasive and nondestructive spectroscopic technique for elemental analysis. In LIBS, short laser pulses are focused onto the sample surface to generate a transient plasma and the complex emission spectra produced during plasma cooling are subsequently analyzed to determine the chemical composition of the material. Owing to its rapid data acquisition and high analytical sensitivity, LIBS has been widely applied in diverse fields, including industrial inspection[8], planetary exploration[9], geological investigation[10], biomedicine[11], food safety[12], and environmental monitoring [13].

Fiber-optic laser-induced breakdown spectroscopy (FO-LIBS), as an emerging branch of LIBS-based detection techniques, integrates optical fiber transmission with conventional LIBS for spectroscopic analysis. In this system, optical fibers are employed to remotely deliver laser energy to the target and to collect the plasma emission for subsequent spectral analysis. Compared with conventional open-path LIBS systems, FO-LIBS offers a compact configuration, flexible optical layout, and strong resistance to environmental interference, enabling real-time multielement detection under harsh conditions such as high temperature, high pressure, and radiation environments[14]. FO-LIBS overcomes the environmental constraints of conventional detection techniques and demonstrates strong potential for in situ applications.

Matrix effects frequently arise in LIBS analysis of solid samples, particularly metals. Even when the elemental concentrations remain unchanged, variations in elemental distribution and microstructural characteristics of the sample can significantly influence the spectral response. Matrix effects are generally classified into chemical matrix effects and physical matrix effects[15]. Chemical matrix effects originate from interactions among elemental species, which alter the emission behavior of the analyte elements[16]. In contrast, physical matrix effects are primarily associated with differences in surface quality and microstructural features of the sample[17].

Matrix effects in LIBS pose a critical challenge to the quantitative determination of elemental concentrations. Matrix-dependent factors often degrade the accuracy and reproducibility of quantitative LIBS measurements. To mitigate these effects, numerous correction strategies have been proposed. Jian *et al.* (2026) introduced a dynamic vision sensor (DVS) to acquire plasma event data and developed a physics-constrained DVS–TI spectral correction model. Experimental results demonstrated that this approach effectively suppresses signal instability caused by matrix-induced variations[18]. In a subsequent study, the same group (2025) further integrated DVS with deep learning techniques by jointly exploiting plasma event–reconstructed images and LIBS spectral information, leading to the development of a temporal spatial attention fusion network (TSAF Net). Under complex operating conditions, such as laser energy fluctuations, the proposed model exhibited a marked improvement in classification robustness[19].

Zhang *et al.* (2024) developed a plasma-parameter correction method based on plasma image–spectrum fusion (PPC-PISF), in which the total particle number density, plasma temperature, and electron density were normalized using combined spectral and plasma image features[20]. Shao *et al.* (2023) proposed a dual-laser system in which a primary laser generates the plasma plume and a secondary laser re-excites the plume within a controlled chamber, thereby reducing matrix interference and improving spectral repeatability[21]. In addition, a variety of other approaches have been reported, including surface-assisted thin film[22] and instrumental optimization of LIBS systems[23].

In contrast, in the analysis of material physical properties and microstructural characteristics, matrix effects in LIBS should not be regarded as sources of interference, but rather as key spectral responses that contain rich structural and property-related information. These effects directly reflect the influence of microstructural features and physical property variations on plasma behavior, thereby providing a physical basis for characterizing material states and properties using LIBS signals. Aberkane *et al.* (2014) demonstrated a strong linear correlation between surface hardness and plasma temperature in Fe–V–C alloys, with harder samples exhibiting higher excitation temperatures[24]. Similar trends were reported by Panya *et al.* (2023) in geological materials[10]. Galmed *et al.* (2023) investigated the effect of laser pulse duration on hardness estimation. They found that sample hardness was positively correlated with plasma temperature under nanosecond laser excitation, whereas a negative correlation was observed under femtosecond excitation[25]. Mohamed *et al.* (2017) reported a strong linear correlation between the emission intensity ratio of titanium ionic to atomic lines and the Vickers hardness of TC4 alloy, with a coefficient of determination of approximately $R^2 \approx 0.99$[26]. ElFaham *et al.* (2020) obtained consistent results in DIN 50Cr3 spring steel[27]. In addition, Yahiaoui *et al.* (2021) investigated the grain size, crystalline

phases, and porosity of aluminum samples and established linear relationships among the ionic-to-atomic line intensity ratio, electron temperature, and surface hardness[28].

Furthermore, data-driven LIBS approaches have been increasingly applied to the identification and classification of alloys. By integrating LIBS with intelligent data processing algorithms, the technique has evolved from a conventional chemical analysis method—primarily based on qualitative or quantitative elemental identification through selected spectral lines—into a powerful analytical tool for industrial applications, thereby substantially expanding its application scope. Zhou *et al.* (2024) combined LIBS with laser-induced plasma acoustic (LIPA) signals and achieved a classification accuracy of 94.2% for different series of TC4 alloys by fusing spectral radiation information and acoustic frequency-domain features at both the feature and decision levels[29]. Tang *et al.* (2025) further optimized this strategy by addressing echo interference and data redundancy in LIPA signals. They proposed an exp-LIPA processing method that integrates attenuation functions with absolute-value-based feature selection and demonstrated that multimodal fusion of exp-LIPA with LIBS spectra significantly improves the classification accuracy of magnesium alloys[30]. In a subsequent study, a time–frequency dual-domain enhanced acoustic feature extraction model (TFDEAP) was introduced. By selectively amplifying subtle acoustic differences related to material physical properties in both the time and frequency domains, this approach markedly enhanced the classification performance of the LIBS–LIPA method for difficult-to-distinguish aluminum alloys, such as Al 3003 and Al 5052[31]. Cui *et al.* (2024) exploited matrix effects in LIBS to classify steel samples with different microstructures and achieved a classification accuracy of 99% by combining convolutional neural networks (CNNs) with random projection (RP)[32]. Yang *et al.* (2024) proposed an ICA–DNN classification framework for effective discrimination of TC4 alloys with different physicochemical states, yielding an overall classification accuracy of 91%[33]. In addition, Hu *et al.* (2022) applied principal component analysis (PCA) and multiplicative scatter correction (MSC) to preprocess LIBS spectra of 10CL60 steel. When distinguishing different metallographic structures, the classification accuracies reached 100% for the calibration set and 98.4% for the prediction set[34].

To address the limitations of conventional microstructural characterization approaches, this study proposes an intra-spot averaging–based PCA–SVM classification strategy for identifying different heat-treated microstructural states of titanium alloys using FO-LIBS. Multiple laser-induced spectra were acquired at each measurement spot and statistically averaged to suppress pulse-to-pulse random fluctuations in spectral features, thereby enabling the model to focus on common spectral characteristics induced by heat treatment. Principal component analysis (PCA) was subsequently employed for feature dimensionality reduction and a support vector machine (SVM) classifier was constructed to discriminate between different heat-treated microstructural states. This approach provides a promising pathway for the rapid, noncontact identification of heat-treated microstructures in titanium alloys.

EXPERIMENTAL

Instrumentation. A schematic diagram of the experimental setup is shown in Fig. 1. A Nd:YAG fiber-coupled laser (Dawa100, Beamtech Inc., China) with an operating wavelength of 1064 nm, a maximum output pulse energy of 60 mJ, and a pulse width of 9 ns was used in this study. Because the solid-state laser emits a Gaussian beam, the beam center exhibits very high power after lens focusing and direct coupling into an optical fiber can easily cause damage to the fiber end face. To address this issue, a microlens array was used to perform beam shaping and energy homogenization, thereby improving the uniformity of the energy distribution. The shaped beam was then coupled into the optical fiber through a focusing lens.

The laser beam emitted from the output fiber is divergent and was first collimated using a collimating lens to form a parallel beam. The beam was subsequently redirected by a reflecting mirror and focused onto the sample surface using a lens with a diameter of 25.4 mm and a focal length of 60 mm to generate plasma. Meanwhile, an off-axis collection probe captured the plasma emission and transmitted it to a spectrometer (HR-2VIS550-5, Ocean Optics Inc., China) through an optical fiber with a core diameter of 400 μm. The spectrometer is a single-channel device with a spectral resolution of 0.12 nm, covering a wavelength range of 450-650 nm. A digital delay generator (DG535, Stanford Research Systems, USA) was used to control the spectrometer timing. The laser trigger signal was sent to the

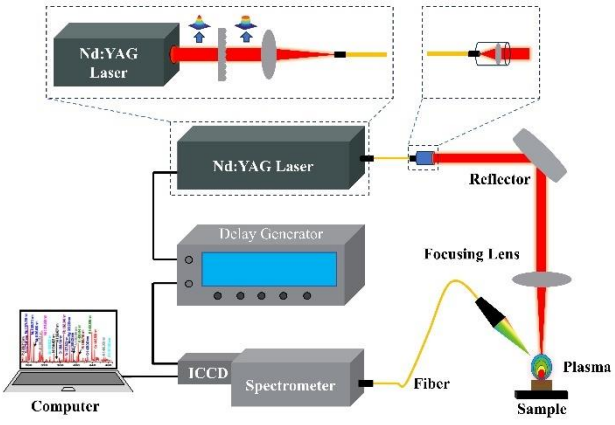

Fig. 1 Schematic diagram of the experimental setup.

delay generator, which subsequently issued a gated acquisition command to the spectrometer after a predefined delay. The integration time and delay time were set to 5 μs and 100 ns, respectively.

Sample preparation. TC4 titanium alloy, with a nominal composition of Ti–6Al–4V, is a typical α+β dual-phase titanium alloy and is well known for its excellent overall mechanical properties. Owing to its good machinability, TC4 is well suited for the fabrication of components with complex geometries, such as aero-engine blades. The chemical composition of the TC4 alloy used in this study is listed in Table 1. To obtain different microstructural states, the samples were subjected to solution treatment followed by aging, as summarized in Table 2.

To eliminate the influence of surface oxides on the measurement results, all samples were subjected to surface pretreatment. The sample surfaces were sequentially polished using silicon carbide abrasive papers with grit sizes ranging from 200 to 2000, followed by fine polishing with a 1 μm diamond polishing paste. The polished surfaces were then thoroughly cleaned with anhydrous ethanol and distilled water.

Methods

Spectral data acquisition. Due to the energy threshold limitation of the optical fiber, the laser pulse energy was set to 40 mJ. The spectrometer separates the plasma emission according to wavelength and measures its intensity. The resulting intensity–wavelength spectral data are subsequently recorded by software.

Considering the possible microscopic heterogeneity of the sample surface, approximately 70 spatially distributed measurement spots were selected for excitation on each of the four heat-treated samples to ensure adequate coverage of the overall sample area and thereby reduce the influence of local compositional fluctuations on the analytical results. In addition, to suppress random fluctuations associated with insufficient pulse numbers, 25 laser pulses were applied at each excitation location. Spectra corresponding to pulses 6–25, after signal stabilization, were selected to construct the surface spectral dataset. This strategy enabled effective representation of microstructural information while significantly reducing random noise.

Standard normal variate spectral normalization (SNV). Min–max normalization is a commonly used spectral intensity scaling method, whose basic principle is to linearly map spectral intensities to a fixed range (typically [0, 1]) to reduce intensity-related differences among samples. However, this approach is sensitive to outliers in the spectrum and primarily performs linear amplitude scaling. As a result, it is often ineffective in suppressing multiplicative interferences arising from surface inhomogeneity, scattering effects, or fluctuations in laser energy.

Table 1. Chemical composition of TC4 alloy (mass fraction, %)

Elements	Content
Ti	Bal.
Al	5.5
V	3.5
Fe	0.096
Si	0.03
Other	0.0778

Table 2. Heat treatment process of four TC4 samples

Elements	Heat treatment process	
	Solid solution treatment	Aging treatment
S1	940°C/1h, Water-cooling	510°C/4h, Air-cooling
S2		570°C/4h, Air-cooling
S3		630°C/4h, Air-cooling
S4		690°C/4h, Air-cooling

Considering the limitations of min–max normalization in handling multiplicative scattering effects and overall spectral shape variations, standard normal variate (SNV) normalization was introduced as an additional spectral preprocessing method[35]. SNV operates on individual spectra by mean centering and standard deviation scaling, thereby effectively reducing variations among samples arising from differences in intensity scale. The mathematical formulation of SNV normalization is given as follows:

$$x_i^{SNV} = \frac{x_i - \bar{x}}{s} \quad (1)$$

Principal component analysis (PCA). Principal component analysis (PCA) is a widely used unsupervised linear dimensionality reduction technique that has been extensively applied in high-dimensional data analysis, feature extraction, and data visualization. The fundamental idea of PCA is to project the original high-dimensional variables onto a set of mutually orthogonal axes through a linear transformation, where the resulting principal components are ordered according to the amount of variance they explain. The first principal component represents the direction of maximum variance and captures the most significant information in the data. Subsequent components are constrained to be orthogonal to the preceding ones and successively maximize the remaining variance. By retaining only the leading principal components, PCA enables effective dimensionality reduction while preserving most of the information contained in the original dataset.

In spectral analysis, spectral data are typically characterized by high dimensionality and strong correlations among variables, which can introduce redundancy and increase computational complexity when modeled directly. PCA not only reduces data dimensionality and suppresses noise but also effectively alleviates multicollinearity among variables, thereby improving the stability and generalization performance of subsequent classification or regression models. Therefore, PCA is employed as a feature

extraction step prior to spectral modeling for spectral classification and quantitative analysis in this study.

Support vector machine (SVM). Support vector machine (SVM) have been widely applied in spectral analysis owing to their strong generalization capability and robustness in high-dimensional, small-sample modeling scenarios. The fundamental principle of SVM is to construct an optimal separating hyperplane in the feature space by maximizing the margin between different classes, thereby achieving effective discrimination among samples. To allow for a certain degree of misclassification, slack variables are introduced, and the optimal solution is obtained based on the structural risk minimization principle. The corresponding optimization objective function can be expressed as follows:

$$\min_{w,b,\xi}\left(\frac{1}{2}||w||^2 + \mathrm{C}\sum_{i=1}^{n}\xi_i\right) \qquad (2)$$

where C is the penalty parameter that balances margin maximization and misclassification penalty, thus controlling the model complexity.

In practical LIBS spectral analysis, sample features often exhibit pronounced nonlinear distribution characteristics. To address this issue, SVM employs kernel functions to implicitly map data into a high-dimensional feature space, enabling nonlinear classification. Given its flexibility and stability in capturing local nonlinear features, the radial basis function (Radial Basis Function, RBF) kernel is adopted in this study to construct the SVM classification model. The kernel function is defined as:

$$K(x_i, x_j) = exp(-\gamma||x_i - x_j||^2) \qquad (3)$$

where γ denotes the kernel parameter, which determines the influence range of individual samples in the feature space.

In view of the high dimensionality of LIBS spectral data, the limited number of samples, and the strong correlations among variables, PCA was introduced to reduce the dimensionality of the original spectra and to extract low-dimensional features that capture the major spectral variations. On this basis, a SVM-based classification model was constructed to fully exploit its classification advantages under high-dimensional, small-sample conditions, thereby enabling effective discrimination of samples with different heat-treatment states. The specific workflow of the study is illustrated in Fig. 2.

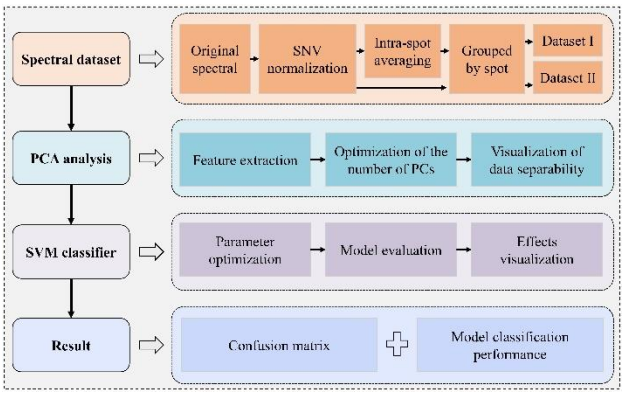

Fig. 2 Flowchart of the classification model combining PCA-SVM with LIBS spectral data.

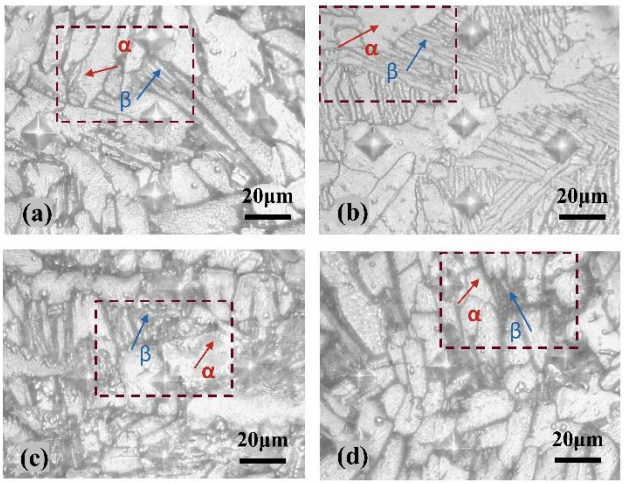

Fig. 3 Microstructures of TC4 alloy solution-treated at 940°C and water-quenched, followed by aging at different temperatures. (a) 510°C; (b) 570°C; (c) 630°C; (d) 690°C.

RESULTS AND DISCUSSION

Analysis of microstructure. When titanium alloys are solution-treated at high temperatures within the β phase field, significant grain coarsening occurs. When the temperature exceeds approximately 1000–1100 °C, excessive grain growth leads to a pronounced deterioration in toughness, a phenomenon commonly referred to as β brittleness. Consequently, the solution treatment temperature for titanium alloys is typically selected within the α + β two-phase region. For TC4 alloy, the β-transus temperature lies in the range of 980–1000 °C. Based on these considerations, a solution treatment temperature of 940 °C was selected in this study. At this temperature, the alloy remains within the α + β two-phase field, allowing partial retention of primary α phase (α_p). During subsequent rapid cooling, the β phase transforms into martensitic α′, resulting in a fine microstructure characterized by relatively high hardness and strength. During the following aging treatment, the α′ martensite and metastable β phase decompose into secondary α phase (α_s) and stable β phase, accompanied by microstructural refinement and stabilization.

Fig. 3 presents the microstructural characteristics of TC4 alloy solution-treated at 940 °C and water-quenched, followed by aging

at different temperatures. Under all aging conditions, the samples exhibit a typical α + β dual-phase microstructure, in which the bright regions correspond predominantly to the α phase, while the darker regions represent the β matrix. As shown in Figs. 3(a) and (b), under low-temperature aging conditions, a relatively high fraction of αp phase is retained, appearing mainly in equiaxed or near-equiaxed morphologies that form the primary structural framework. Meanwhile, a large number of fine and uniformly distributed lamellar α_s phase precipitates within the β matrix, leading to a dense transformed microstructure with an increased density of α/β phase boundaries. The dispersed distribution of fine secondary α phase effectively impedes dislocation motion and constitutes a key strengthening mechanism under low-temperature aging conditions. With further increases in aging temperature, as shown in Figs. 3(c) and 3(d), the α_s phase precipitated within the β phase undergoes pronounced coarsening and coalescence, manifested by increased lamellar thickness and spacing. Concurrently, the number of α/β phase boundaries decreases, and the microstructure gradually evolves from a strengthened state toward a more stable configuration.

LIBS spectral analysis. Fig. 4 shows the LIBS spectra corresponding to the 15th laser pulse selected from representative measurement spots of four samples. After standard normal variate (SNV) normalization, differences in spectral profiles can be clearly observed. As illustrated in the figure, the dominant spectral features are mainly distributed within the wavelength range of 450–650 nm. Accordingly, the present study focuses on the analysis of spectral signals in this region. The major emission peaks are concentrated in the ranges of 452–457 nm, 495–506 nm, and 517–523 nm, which are highlighted by gray shaded areas in the figure. Within these wavelength intervals, the relative intensities of certain ionic emission lines (*e.g.*, Fe II at 564.3 nm) exhibit systematic variations with aging temperature. This behavior is closely associated with differences in mechanical properties arising from microstructural evolution of the TC4 alloy under different heat-treatment conditions. As discussed previously, during low-temperature aging, a large number of fine and uniformly dispersed α_s phase precipitates within the β matrix, leading to increased strength and hardness, which in turn promotes plasma excitation and ionization[36, 37]. In contrast, under high-temperature aging conditions, coarsening of the secondary α phase enhances material ductility and toughness, resulting in a relatively reduced degree of plasma ionization. These microstructure-induced variations in mechanical properties alter plasma ionization behavior and are ultimately manifested as systematic changes in the relative intensities of ionic emission lines.

In addition, heat treatment induces variations in elemental distribution, which in turn influence the LIBS spectra. The mechanical properties of metallic materials are governed by their microstructure, and in dual-phase titanium alloys, elemental partitioning plays a critical role in determining both microstructural

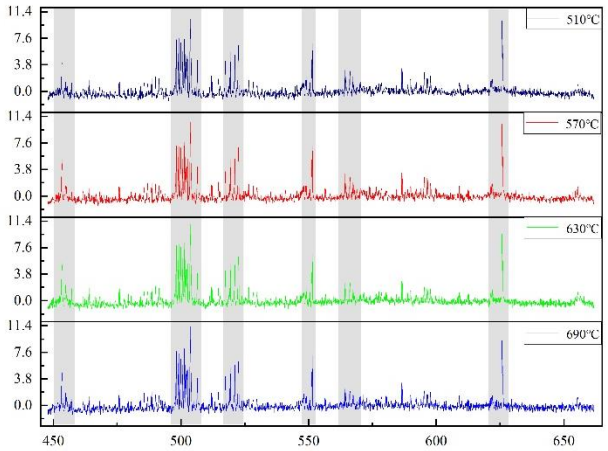

Fig. 4 LIBS spectra of TC4 titanium alloy under four different heat treatment conditions.

characteristics and mechanical performance[38, 39]. Popov et al. reported that the quenching temperature significantly affects the lattice parameters and phase dimensions of quenched martensite in VT16 alloy, primarily due to changes in the content of stabilizing elements within the β phase[39]. Elemental redistribution influences the morphology and distribution of the α and β phases, the modes of plastic deformation, and ultimately the mechanical properties of the alloy. Consequently, when samples are analyzed using LIBS, heterogeneity in elemental distribution leads to discernible differences in the resulting characteristic spectra among samples.

However, from a macroscopic perspective, the spectra of the four samples do not exhibit pronounced differences. Microstructural changes induced by heat treatment arise from the coupling of multiple factors, and their influence on LIBS spectra is not confined to a single emission line or a specific spectral band. Instead, these effects are subtly distributed across multiple characteristic wavelengths as weak spectral variations. In addition, pulse-to-pulse plasma fluctuations and experimental noise further complicate visual interpretation. Moreover, these spectral differences lack clearly observable patterns and cannot generally be quantified or classified using prior information, such as formulas. In contrast, data-driven machine learning approaches enable the joint modeling of multivariate spectral information and can amplify subtle spectral differences associated with heat treatment by learning statistical patterns across samples. Accordingly, this study employs a combined PCA and SVM framework to identify the heat-treatment states of titanium alloys.

Pulse-level spectral classification. For each measurement point, 20 pulse spectra acquired after the initial ablation stage were selected for analysis, with each pulse spectrum treated as an individual sample. To reduce the influence of overall signal intensity fluctuations on classification performance, all pulse-level

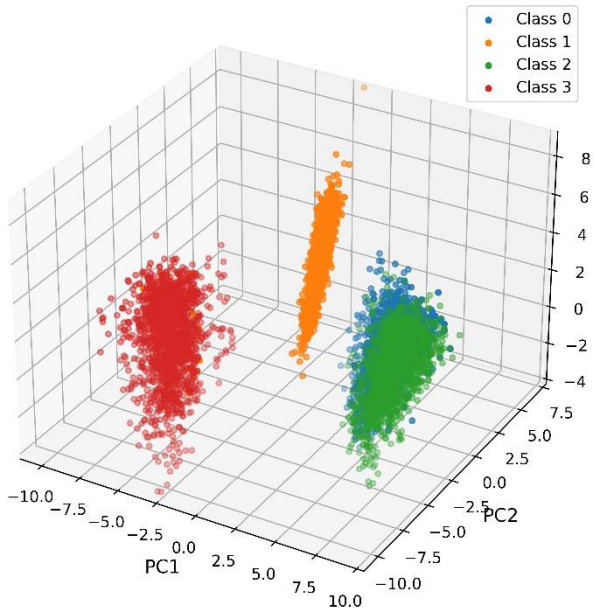

Fig. 5 3D distribution of pulse-level spectra of the samples in principal component space.

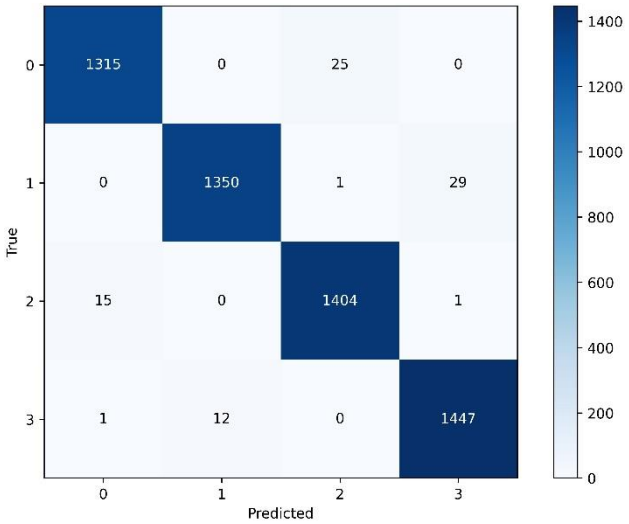

Fig. 6 Confusion matrix of pulse-level spectra classification.

spectra were normalized using the standard normal variate (SNV) method prior to model construction. PCA was then applied to reduce the dimensionality of the high-dimensional spectral data, followed by the construction of a SVM classifier with a radial basis function (RBF) kernel in the principal component space.

Given the limited number of samples, a five-fold cross-validation (K = 5) strategy was employed to evaluate the classification performance. In each fold, the model was trained on the training subset and tested on the validation subset, and the final performance metrics were obtained by aggregating the results across all folds. Because multiple pulse spectra acquired at the same measurement point are highly correlated in both physical and statistical terms, they cannot be regarded as independent samples. Randomly assigning pulse spectra from the same measurement point to both training and validation sets may lead to data leakage and, consequently, an overestimation of model performance. To address this issue, a grouped cross-validation scheme was adopted. All pulse spectra acquired from the same measurement point were assigned to a single group, ensuring that spectra from a given point appeared exclusively in either the training set or the validation set in each fold. This validation strategy enables a more realistic assessment of the model's generalization capability to unseen measurement points.

Figure 5 illustrates the three-dimensional distribution of pulse-level SNV-normalized spectra projected onto the first three principal components. As shown, samples from different classes exhibit a certain degree of clustering in the low-dimensional feature space, particularly for Classes 1 and 3. However, noticeable within-class dispersion is also observed, reflecting the inherent random fluctuations present in pulse-level spectra. In addition, Classes 0 and 2 exhibit substantial overlap in this space, indicating limited separability in the low-dimensional principal component space. Their discriminative information may be distributed across higher-order principal components and nonlinear features, requiring further discrimination.

On this basis, the classification performance of pulse-level spectra was evaluated under a grouped cross-validation scheme and statistically summarized using a confusion matrix, as shown in Fig. 6. By ensuring that pulse spectra acquired from the same measurement point were not simultaneously used for training and testing, this evaluation strategy provides a more rigorous assessment of the model's classification performance.

The classification accuracy of the model was calculated based on the confusion matrix and is defined as:

$$Accuracy = \frac{TP + TN}{TP + TN + FP + FN} \quad (4)$$

Where TP, TN, FP, FN,denote true positives, true negatives, false positives, and false negatives, respectively. Based on this metric, the pulse-level PCA–SVM model achieved a prediction accuracy of 98.5%.

Pulse-level LIBS spectra acquired consecutively at a single measurement point typically exhibit pronounced pulse-to-pulse fluctuations. These fluctuations mainly arise from variations in laser pulse energy, instability during plasma formation, and local heterogeneity of the sample surface. Consequently, although using single-pulse spectra for classification preserves the maximum amount of raw measurement information, it also imposes more stringent requirements on model robustness.

Overall, pulse-level spectral classification indicates that individual LIBS spectra contain discriminative information related to sample treatment states, but they are susceptible to random fluctuations. Therefore, further suppression of pulse-to-pulse variability is necessary to enhance the stability and reliability of the classification model.

Spectral classification based on intra-spot averaging. Heat treatment induces systematic microstructural evolution by regulating phase constitution, precipitation behavior, and defect structures within materials. In LIBS, such evolution is typically manifested as global variations in spectral line intensities, relative peak ratios, and continuum background characteristics. Unlike the random fluctuations caused by plasma instability and measurement noise during single-pulse laser ablation, heat-treatment-induced spectral variations exhibit statistical consistency and reproducibility, reflecting intrinsic material states at the spectral level. Therefore, classification modeling of heat-treatment states should focus on extracting and characterizing these stable, shared spectral features rather than relying on highly unstable transient information contained in single-pulse spectra.

As observed in the pulse-level spectral classification results discussed above, individual pulse spectra contain a certain degree of discriminative information. However, pulse-to-pulse fluctuations may partially obscure the common spectral characteristics associated with different heat-treatment conditions. Consequently, classification models must operate under a relatively high noise background, which increases the difficulty of discrimination and may adversely affect the identification accuracy of the model. In contrast, statistical averaging of multiple pulse spectra acquired at the same measurement point can effectively suppress random noise and transient fluctuations while preserving heat-treatment-related information, thereby facilitating the identification of intrinsic differences among heat-treatment states. On this basis, intra-spot spectral averaging was adopted as a noise suppression strategy, and a PCA–SVM classification model was subsequently constructed to systematically analyze different heat-treatment conditions.

In practice, multiple pulse-level LIBS spectra were consecutively acquired at each measurement point, and spectra corresponding to a relatively stable plasma state after the initial ablation stage were selected for analysis. Each pulse spectrum was first subjected to standard normal variate (SNV) normalization to mitigate the effects of laser energy fluctuations and overall signal intensity variations. Subsequently, intra-spot averaging was applied to the normalized spectra, as expressed by the following equation:

$$\bar{I}(\lambda_j) = \frac{1}{N}\sum_{i=1}^{N} I_i(\lambda_j), j = 1,2,\dots,M \qquad (5)$$

where $I_i(\lambda_j)$, $\bar{I}(\lambda_j)$ denote the spectral intensities at wavelength λ_j before and after intra-spot averaging, respectively; N represents the number of pulses acquired at a given measurement spot, and M denotes the total number of wavelength points in the spectrum. Intra-spot spectral averaging effectively suppresses pulse-to-pulse random fluctuations in spectral profiles, thereby enhancing microstructure-related features induced by heat treatment and yielding a representative spectrum that characterizes the overall spectral response of the measurement spot.

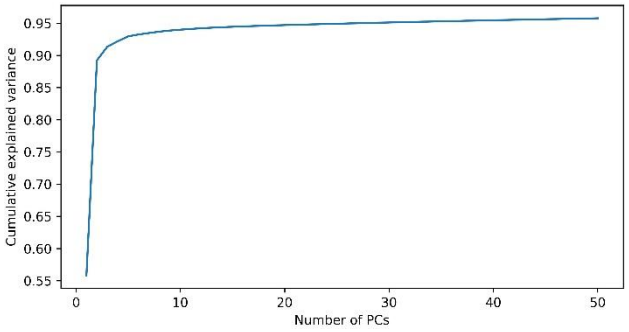

Fig. 7 Relationship between cumulative explained variance and the number of principal components.

After obtaining the intra-spot averaged spectra, PCA was applied to reduce the dimensionality of the high-dimensional spectral data. In this study, the number of principal components was determined by jointly considering the cumulative explained variance and the stability of classification performance. As shown in Fig. 7, the cumulative explained variance analysis indicates that the first 10 principal components account for approximately 90% of the total variance. When the number of principal components increases to around 20, the cumulative explained variance exceeds 93%, suggesting that the major spectral information has been adequately captured. Further increasing the number of principal components to 40–50 results in only a marginal gain in cumulative explained variance (approximately 2%), with the additional components mainly representing low-variance information or noise, which may introduce redundancy and increase model complexity, thereby adversely affecting model generalization. Based on these considerations, the number of principal components was restricted to the range of [10, 30], and the final selection was determined using cross-validation to identify the number that provides stable and superior classification performance for subsequent modeling.

Figure. 8 presents the three-dimensional distribution of intra-spot averaged spectra from four sample classes in the space defined by the first three principal components. As observed, samples corresponding to different heat-treatment conditions exhibit clear clustering behavior in the reduced feature space. Compared with pulse-level spectra, intra-spot averaged spectra

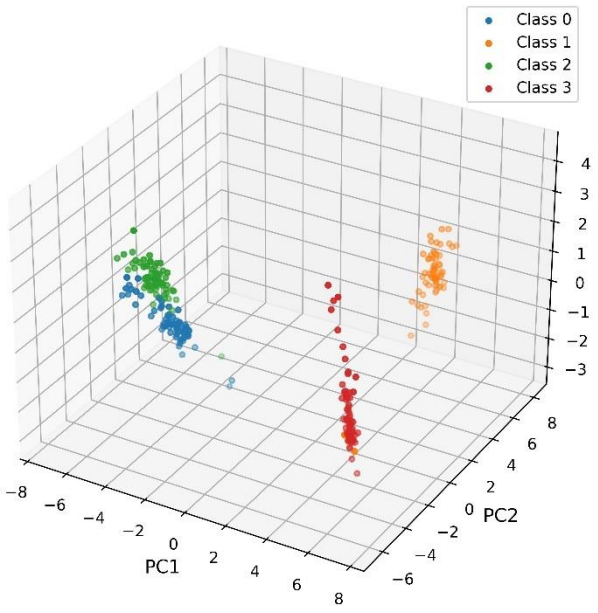

Fig. 8 3D distribution of within-spot averaged sample spectra in principal component space.

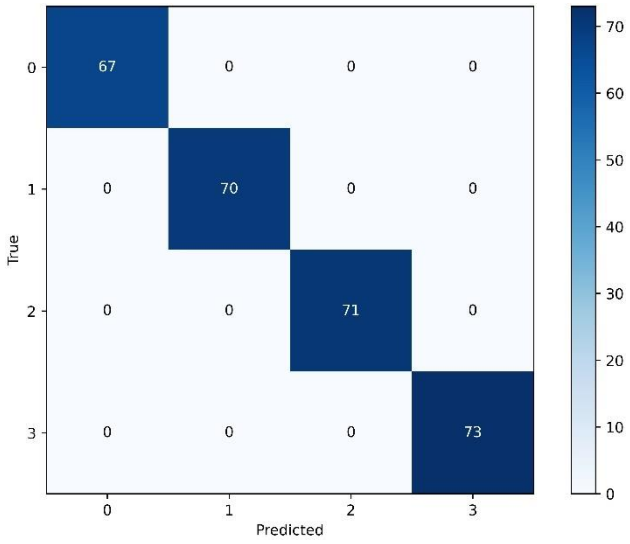

Fig. 9 Confusion matrix of classification results for within-spot averaged sample spectra.

show more pronounced clustering and substantially enhanced inter-class separability in the low-dimensional principal component space. Although partial overlap between Classes 0 and 2 remains, their overall distributions display a clearer boundary, which is favorable for subsequent classification. These results demonstrate that intra-spot averaging effectively suppresses pulse-to-pulse random fluctuations, enhances shared spectral features induced by heat treatment, and significantly improves separability in the feature space.

On this basis, a SVM classification model with a radial basis function (RBF) kernel was constructed in the PCA-reduced feature space. The performance of the RBF-SVM model is mainly governed by the penalty parameter C and the kernel parameter γ. Specifically, C controls the trade-off between maximizing the classification margin and penalizing training errors, thereby regulating model complexity. γ determines the influence range of samples in the high-dimensional feature space and plays a critical role in the smoothness and local discriminative capability of the decision boundary. In this study, a grid search combined with cross-validation was employed to systematically optimize C and γ. Taking into account the scale characteristics of the PCA-reduced feature space and the observed model performance, the search range of C was restricted to [10, 100], with a denser search conducted in performance-sensitive regions, while γ was limited to the order of magnitude of 10^{-3}-10^{-1}. During hyperparameter optimization, the macro-averaged F1 score (macro-F1) was adopted as the evaluation metric, and the parameter combination yielding the highest and most stable average macro-F1 score under cross-validation was selected as optimal. The final model parameters were determined as $n\_components = 14$, $C = 50$ and $\gamma = 0.013$.

Classification performance was evaluated based on cross-validation predictions, and the corresponding confusion matrix is shown in Fig. 9. The results indicate that all heat-treatment states were identified with high accuracy, with four states achieving an accuracy of 100%. Moreover, the overall misclassification rate was lower than that obtained using pulse-level grouped classification, demonstrating that the intra-spot averaged PCA–SVM approach offers clear advantages in terms of classification stability and reliability.

Based on the above analysis, intra-spot spectral averaging enables the classification model to focus on stable spectral features associated with differences in heat-treatment states, rather than being dominated by unavoidable random fluctuations arising from individual laser ablation events. Consequently, compared with pulse-level grouped classification, the intra-spot averaged PCA–SVM approach not only achieves superior classification performance but also demonstrates clearer physical interpretability and greater engineering feasibility, making it a more suitable method for heat-treatment state identification.

Classification of eight different heat-treated microstructures. In the preceding analysis, the intra-spot averaged PCA–SVM approach was demonstrated to effectively distinguish samples subjected to different heat-treatment conditions and to exhibit advantages in suppressing spectral noise and improving classification stability. However, these results were primarily obtained under scenarios involving a small number of classes. As

the number of sample types and processing conditions increases, spectral differences among classes tend to become more complex, and class boundaries increasingly overlap, thereby imposing greater demands on the discriminative capability and generalization performance of classification models. It is therefore necessary to further evaluate the applicability of the proposed method under conditions involving a larger number of classes.

Accordingly, this study extends the intra-spot averaged PCA–SVM classification framework to a multiclass task comprising eight distinct heat-treatment conditions to assess its effectiveness in more complex classification scenarios. Compared with low-class-number classification, the eight-class classification problem introduces additional overlapping regions in the feature space, requiring the model not only to capture the dominant differences among sample states but also to maintain stable discrimination capability under multiclass conditions.

Figure 10 illustrates the distribution of intra-spot averaged spectra from the eight sample classes projected onto the first three principal components. Although the increased number of classes leads to a more complex feature space structure, samples from different classes still exhibit a certain degree of clustering in the principal component space. This observation indicates that the proposed method remains effective in enhancing spectral separability under multiclass conditions.

On this basis, a SVM model was employed to classify the eight sample categories, and the optimal model parameters were determined as $n\_components = 16$, $C = 50$ and $\gamma = 0.017$. The corresponding cross-validation prediction results are shown in Fig. 11. As indicated by the confusion matrix, the model achieved an overall classification accuracy of 99.8%, with the majority of sample classes being accurately distinguished, demonstrating stable and excellent classification performance.

Comparison with the previously reported results obtained for fewer classes indicates that despite the substantially increased difficulty of the classification task, the intra-spot averaged PCA–SVM approach maintains strong overall discriminative capability and classification stability. This finding suggests that the proposed method does not rely on a specific number of classes or simplified classification scenarios, but is instead capable of robustly extracting the principal spectral features that reflect differences in sample states as the class scale increases.

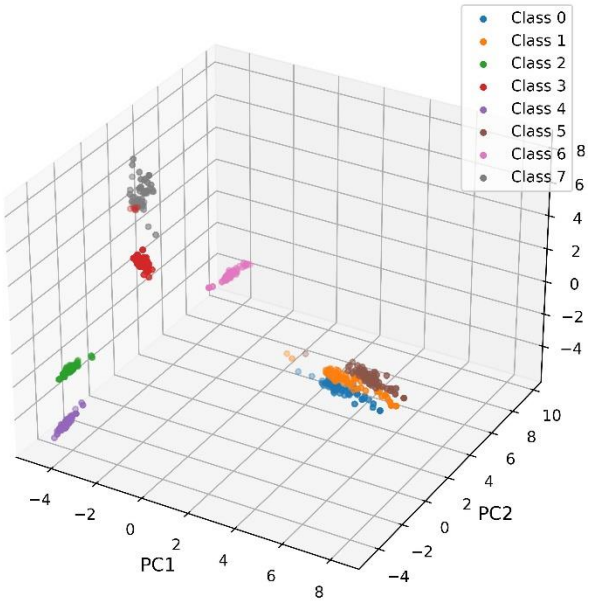

Fig. 10 3D distribution of spectra from eight sample classes in principal component space.

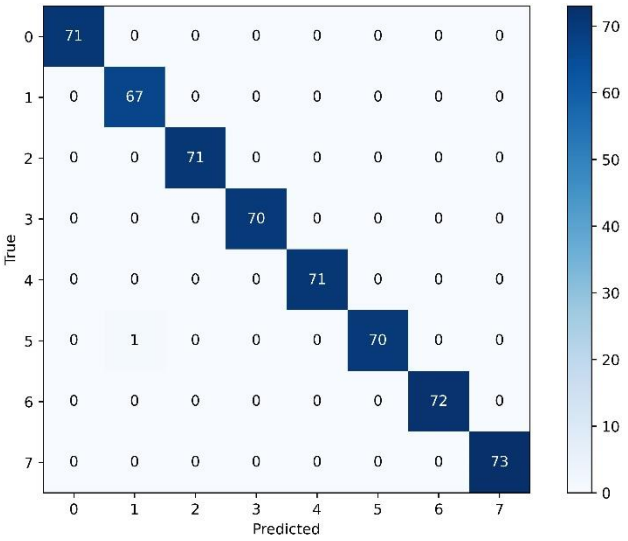

Fig. 11 Confusion matrix of classification results for eight types of sample spectra.

CONCLUSION

To address the rapid identification of different heat-treatment-induced microstructural states in TC4 titanium alloy, a classification approach combining FO-LIBS, PCA, and SVM was developed in this study. LIBS spectra were acquired at multiple spatially distributed measurement points on the sample surface, thereby improving sampling representativeness. The results of the pulse-level classification method indicate that single-pulse LIBS spectra inherently contain characteristic information related to heat-treatment states. However, the classification performance of this approach may be affected by pulse-to-pulse random fluctuations. To mitigate this issue, an intra-spot multi-pulse spectral averaging strategy was introduced to suppress random fluctuations and enhance the stability of spectral features, enabling

the model to focus on spectral variations induced by heat treatment. PCA was subsequently employed for feature extraction, followed by SVM-based classification. Under grouped cross-validation conditions, high-accuracy identification of different heat-treatment states of TC4 titanium alloy was achieved, with intra-spot averaged spectra outperforming pulse-level analysis. Accuracies reached 100% for the four-class classification task and 99.8% for the eight-class classification task. These results demonstrate that the combination of appropriate spectral preprocessing and data-driven modeling enables LIBS to effectively discriminate heat-treatment states of titanium alloys. Moreover, LIBS achieves high classification accuracy while maintaining detection efficiency, suggesting its potential as a practical technique for the rapid identification of material microstructural states.

AUTHOR INFORMATION

Dan Feng, currently an Associate Researcher at Northwestern Polytechnical University. She received her Bachelor's Degree from the School of Physics and Information Technology, Shaanxi Normal University in 2013, and was recommended for admission to Xi'an Jiaotong University to pursue her Ph.D. degree without taking the entrance examination. She conducted joint training at Southern University of Science and Technology from 2015 to 2018, and obtained her Ph.D. degree in Materials Science and Engineering from Xi'an Jiaotong University in 2018. Since taking up her current position, she has been engaged in the research on advanced characterization and testing methods for high-performance metallic materials for aerospace applications. She is responsible for the research on characterization technologies and the development of in-situ experiments for the double spherical aberration-corrected transmission electron microscope, focused ion/electron dual-beam electron microscope, micro-Raman confocal spectrometer, laser-induced breakdown spectroscopy system, and other advanced instruments. She has participated as a core member in the General Program of the National Natural Science Foundation of China. She has published 5 SCI papers as the first author, one of which was selected as the cover article of the journal. Through the research on advanced characterization technologies and the development of related experiments, she has provided technical support for the publication of relevant research results in top journals in the materials field such as *Acta Materialia* and *Angewandte Chemie*.

Minchao Cui, Ph.D. in Mechanical Engineering from Xi'an Jiaotong University (China), Ph.D. in Intelligent Mechanical Systems from The University of Tokushima (Japan), Winner of the China Youth Science and Technology Innovation Award. He previously served as Professor and Ph.D. Supervisor at Northwestern Polytechnical University, and currently holds the position of Senior Researcher at the National Innovation Center for Digital Design and Manufacturing. He has been selected for the 9th Young Talent Support Program of the China Association for Science and Technology, Distinguished Young Scholar of the Frontiers of Chinese Engineering by the Chinese Academy of Engineering, High-level Talent Program of Qinchuangyuan in Shaanxi Province, and Young Talent Support Program of the Shaanxi Association for Science and Technology. His main research interests focus on pulsed laser sensing technology, laser-induced active photoacoustic fusion theory, and data intelligent processing algorithms. He has successively presided over a series of national research projects, including research topics of National Major Science and Technology Special Projects, General Programs and Young Scientists Fund of the National Natural Science Foundation of China, sub-topics of the National Major Science and Technology Special Project for Aero-engines and Gas Turbines, Key Projects of the Basic Science Center for Aero-engines and Gas Turbines, as well as General Programs of the China Postdoctoral Science Foundation. He has published more than 40 SCI papers as the first or corresponding author (5 of which are listed as ESI Highly Cited Papers), and obtained 14 authorized national invention patents as the first inventor. He is a Senior Member of the Chinese Optical Society, a Senior Member of the Chinese Society for Graphics, and a Young Editorial Board Member of *Metallurgical Analysis*.

Corresponding Author

* D. Feng

Email address: fengd@nwpu.edu.cn

* M. C. Cui

Email address: cuiminchao@nwpu.edu.cn

Notes

The authors declare no competing financial interest.

ACKNOWLEDGMENTS

This work was co-supported by the National Natural Science Foundation of China (62375221), National Key Research and Development Program of China (2024YFB4710502), Fundamental Research Funds for the Central Universities (D5000240083), Science Fund Program for Excellent Young Scientists, Qinchuangyuan Support Plan in Shaanxi Province of China (QCYRCXM-2022-132), Young Elite Scientists Sponsorship Program by CAST (YESS20230266), Fundamental Research Funds for the Central Universities and Innovation Capability Support Program of Shaanxi (2022TD-60).

REFERENCES

1. R. Kumar, S. Roy, P. Gunjan, A. Sahoo, D. D. Sarkar and R. K. Das, *Procedia Manuf.*, 2018, **20**, 358-364. https://doi.org/10.1016/j.promfg.2018.02.052
2. R. Kumar, A. K. Sahoo, K. Satyanarayana and G. Rao, *Int. J. Ind. Eng. Comput.*, 2013, **4**, 427-436. https://doi.org/10.5267/j.ijiec.2013.03.002
3. M. Geetha, A. K. Singh, R. Asokamani and A. K. Gogia, *Prog. Mater. Sci.*, 2009, **54**, 397-425. https://doi.org/10.1016/j.pmatsci.2008.06.004

4. B. Venkatesh, D. Chen and S. Bhole, *Mater. Sci. Eng: A*, 2009, **506**, 117-124. https://doi.org/10.1016/j.msea.2008.11.018
5. M. Rizwan, R. Ullah, J. Lu, J. Wang, Y. Zhang and Z. Zhang, *Mater. Sci. Eng: A*, 2024, **914**, 147163. https://doi.org/10.1016/j.msea.2024.147163
6. K. Han, S. Qin, H. Li, J. Liu, Y. Wang, C. Zhang, P. Zhang, S. Zhang, H. Zhang and H. Zhou, *Mater. Charact.*, 2019, **158**, 109936. https://doi.org/10.1016/j.matchar.2019.109936
7. E. S. N. Lopes, A. Cremasco, C. R. M. Afonso and R. Caram, *Mater. Charact.*, 2011, **62**, 673-680. https://doi.org/10.1016/j.matchar.2011.04.015
8. J. D. Pedarnig, S. Trautner, S. Grünberger, N. Giannakaris, S. Eschlböck-Fuchs and J. Hofstadler, *Appl. Sci.*, 2021, **11**, 9274. https://doi.org/10.3390/app11199274
9. R. Gaudiuso, M. Dell'Aglio, O. De Pascale, G. S. Senesi and A. De Giacomo, *ACS Sens.*, 2010, **10**, 7434-7468. https://doi.org/10.3390/s100807434
10. S. N. Panya panya, A. H. Galmed, M. Maaza, B. M. Mothudi and M. A. Harith, *Mater. Today: Proc.*, 2021, **36**, 600-603. https://doi.org/10.1016/j.matpr.2020.05.766
11. J. Lin, Y. Li, X. Lin and C. Che, *Anal. Bioanal. Chem.*, 2024, **416**, 993-1000. https://doi.org/10.1007/s00216-023-05089-5
12. Y. G. M. Kongbonga, H. Ghalila, M. B. Onana and Z. B. Lakhdar, *Food Chem.*, 2014, **147**, 327-331. https://doi.org/10.1016/j.foodchem.2013.09.145
13. E. C. Ferreira, E. J. Ferreira, P. R. Villas-Boas, G. S. Senesi, C. M. Carvalho, R. A. Romano, L. Martin-Neto and D. M. B. P. Milori, *Spectrochim. Acta B*, 2014, **99**, 76-81. https://doi.org/10.1016/j.sab.2014.06.016
14. R. Nakanishi, M. Saeki, I. Wakaida and H. Ohba, *Appl. Sci.*, 2020, **10**, 8985. https://doi.org/10.3390/app10248985
15. W. Xu, C. Sun, Y. Tan, L. Gao, Y. Zhang, Z. Yue, S. Shabbir, M. Wu, L. Zou, F. Chen, S. Liu and J. Yu, *J. Anal. At. Spectrom.*, 2020, **35**, 1641-1653. https://doi.org/10.1039/D0JA00157K
16. T. Takahashi and B. Thornton, *Spectrochim. Acta B*, 2017, **138**, 31-42. https://doi.org/10.1016/j.sab.2017.09.010
17. S. Shabbir, Y. Zhang, C. Sun, Z. Yue, W. Xu, L. Zou, F. Chen and J. Yu, *J. Anal. At. Spectrom.*, 2021, **36**, 1441-1454. https://doi.org/10.1039/D1JA00076D
18. H. Jian, L. Deng, X. Wang, Q. Lyv, H. Yuan, J. Wang, X. Wang and Z. Jia, *Measurement*, 2026, **257**, 118782. http://doi.org/10.1016/j.measurement.2025.118782
19. H. Jian, L. Deng, J. Wang, Z. Shen, X. Wang and Z. Jia, *J. Anal. At. Spectrom.*, 2025, **40**, 2658-2672. http://doi.org/10.1039/d5ja00238a
20. D. Zhang, X. Niu, J. Nie, S. Shi, H. Ma and L. Guo, *Opt. Express*, 2024, **32**, 10851-10861. https://doi.org/10.1364/OE.515064
21. J. Shao, Y. Zhang and A. Chen, *ACS Photonics*, 2023, **10**, 783. https://doi.org/10.3390/photonics10070783
22. Y. Tian, H. C. Cheung, R. Zheng, Q. Ma, Y. Chen, N. Delepine-Gilon and J. Yu, *Spectrochim. Acta B*, 2016, **124**, 16-24. https://doi.org/10.1016/j.sab.2016.08.016
23. B. C. Windom and D. W. Hahn, *J. Anal. At. Spectrom.*, 2009, **24**, 1665-1675. https://doi.org/10.1039/B913495F
24. S. M. Aberkane, A. Bendib, K. Yahiaoui, S. Boudjemai, S. Abdelli-Messaci, T. Kerdja, S. Amara and M. Harith, *Appl. Surf. Sci.*, 2014, **301**, 225-229. https://doi.org/10.1016/j.apsusc.2014.02.046
25. A. Galmed, O. Balachninaite and O. A. Nassef, *Opt. Laser Technol.*, 2023, **161**, 109184. https://doi.org/10.1016/j.optlastec.2023.109184
26. G. A. H. Mohamed D. F, Nassef, *Arab. J. Nucl. Sci. Appl.*, 2017, 142-155.
27. M. M. ElFaham, W. M. Elthalabawy, O. Elzahed, M. A. Zakaria and M. Abdelhamid, *Appl. Phys. A*, 2020, **126**, 167. https://doi.org/10.1007/s00339-020-3348-4
28. K. Yahiaoui, S. Messaoud Aberkane and A. Naitbouda, *Mater. Chem. Phys.*, 2021, **259**, 124045. https://doi.org/10.1016/j.matchemphys.2020.124045
29. J. Zhou, L. Guo, M. Zhang, W. Huang, G. Wang, A. Gong, Y. Liu and H. Sattar, *Anal. Chim. Acta*, 2024, **1309**, 342674. http://doi.org/10.1016/j.aca.2024.342674
30. J. Tang, N. Aizezi, J. Liu, W. Gao and Y. Liu, *Opt. Laser Technol.*, 2025, **192**, 114043. https://doi.org/10.1016/j.optlastec.2025.114043
31. Z. Wang, N. Aizezi, Y. Ye, Y. Chen, J. Li, B. Yu, W. Sun and Y. Liu, *Talanta*, 2026, **300**, 129208. http://doi.org/10.1016/j.talanta.2025.129208
32. M. Cui, G. Shi, L. Deng, H. Guo, S. Xiong, L. Tan, C. Yao, D. Zhang and Y. Deguchi, *J. Anal. At. Spectrom.*, 2024, **39**, 1361-1374. https://doi.org/10.1039/D3JA00453H
33. N. Yang, M. J. Shan, G. Y. Shi, H. R. Guo, S. L. Xiong, M. Luo, D. H. Zhang and M. C. Cui, *Atom. Spectrosc.*, 2024, **45**, 324-335. https://doi.org/10.46770/AS.2024.158
34. H. Jun, Y. Liang, T. Z. Lin, H. Y. Shi, Q. Peng, H. Yong and L. Yande, *Opt. Express*, 2022, **30**, 47970-47982. https://doi.org/10.1364/OE.471222
35. Å. Rinnan, F. v. d. Berg and S. B. Engelsen, *TrAC, Trends Anal. Chem.*, 2009, **28**, 1201-1222. http://doi.org/10.1016/j.trac.2009.07.007
36. K. Tsuyuki, S. Miura, N. Idris, K. H. Kurniawan, T. J. Lie and K. Kagawa, *Appl. Spectrosc.*, 2006, **60**, 61-64. http://doi.org/10.1366/000370206775382668
37. M. M. ElFaham, M. Okil and A. M. Mostafa, *Opt. Laser Technol.*, 2018, **108**, 634-641. http://doi.org/10.1016/j.optlastec.2018.07.022
38. P. Barriobero-Vila, G. Requena, T. Buslaps, M. Alfeld and U. Boesenberg, *J. Alloys Compd.*, 2015, **626**, 330-339. http://doi.org/10.1016/j.jallcom.2014.11.176
39. A. A. Popov, A. G. Illarionov, S. I. Stepanov, O. A. Elkina and O. M. Ivasishin, *Phys. Met. Metallogr.*, 2014, **115**, 507-516. http://doi.org/10.1134/S0031918X14050068